

Numerical modeling of solid oxide fuel cells

Thin X. Ho ^{a,*} Pawel Kosinski ^a Alex C. Hoffmann ^a

Arild Vik ^b

^a*Department of Physics and Technology, University of Bergen,*

Allegt 55, 5007 Bergen, Norway

^b*Prototech AS, Fantoftvegen 38, 5892 Bergen, Norway*

Abstract

This paper presents a numerical model for a planar solid oxide fuel cell (SOFC) with mixed ionic-electronic conducting electrodes. Transport of positive or negative charges, which takes place in the direction of down- or up-gradient electric potential, respectively, within the composite electrodes and through the electrolyte membrane, is mimicked by making use of an algorithm for Fickian diffusion in the commercial software. The output cell voltage, which is the potential difference between the two current collectors, is fixed at a given value. The coupled equations describing the conservation of mass, momentum and energy and the chemical and electrochemical processes are solved using the commercial package Star-CD, augmented with sub-routines developed in-house. Results for the concentration of chemical species and the distributions of temperature and current density in an anode-supported SOFC with direct internal reforming are presented and discussed. The potential for using this model as a general numerical tool to study the impact of the detailed processes taking place in solid oxide fuel cells is discussed.

Key words: SOFC; Composite electrode; Mathematical modeling; Transport

1 Introduction

Solid oxide fuel cells (SOFC) have gained the interest of many researchers because of some clear advantages even compared to other types of fuel cells: high efficiency and the capability of working with a wide range of fuels. Tubular and planar solid oxide fuel cells are the most popular designs. The former one has the advantage that sealing is easier. However, the latter one is superior in terms of efficiency and ease of manufacture and stacking.

The number of SOFC research papers has been considerably increasing during the last two decades. While experimental studies mostly focus on the evaluation of possible materials and/or fuels, numerical studies focus on modeling the coupled physical and chemical and electrochemical phenomena occurring in the cell/stack.

Some studies have used three-dimensional (3D) approaches to model the whole cell/stack (Pasaogullari and Wang, 2003; Petruzzi et al., 2003; Recknagle et al., 2003; Yakabe et al., 2001). In such studies the impact of the configuration and operating conditions (*e.g.* fuel and air inlets) on the overall performance of the cell/stack is among common objectives. However, micro processes or phenomena occurring within the ensemble of positive electrode-electrolyte-negative electrode (PEN) are grossly simplified.

* Corresponding author. Tel: +47 55 57 41 28; Fax: +47 55 57 41 14

Email address: think.ho@ift.uib.no (Think X. Ho)

Two-dimensional (2D) models are popular with tubular solid oxide fuel cells because of their axial symmetry (Janardhanan and Deutschmann, 2006; Klein et al., 2007; Li and Chyu, 2003; Suwanwarangkul et al., 2006). Others have used quasi-2D models planar designs (Janardhanan and Deutschmann, 2007; Zhu et al., 2005). In quasi-2D models, one-dimensional fluid flows in the channels are coupled with the transverse gas transport in the porous electrodes by boundary conditions at the channel-electrode interfaces.

In one-dimensional (1D) approaches the PEN structure is considered as a thin layer separating the fuel and the air channel flows (Aguiar et al., 2004; Inui et al., 2006). Therefore, micro processes happening within the PEN are not observed either.

Another class of studies exists, consisting of studies which do not aim to model the cell as a whole, but focus on the analysis of phenomena occurring locally in the porous electrodes and/or in the electrolyte (Chan et al., 2001; Ciucci and Goodwin, 2007; Fleig, 2002, 2003; Hao and Goodwin, 2007; Kenney and Karan, 2004; Lehnert et al., 2000; Søggaard et al., 2006; Suwanwarangkul et al., 2003; Zhu and Kee, 2007). Polarization mechanisms, charge transfers and heterogeneous reactions are among their interests.

We now focus on the studies most relevant to this work. We need to say here that a state-of-the-art planar SOFC may have two designs: electrolyte- or electrode-supported. The former design comprises a thick electrolyte (120–200 μm), which may produce high ohmic losses especially at low temperature. The later design has a thick anode or cathode depending on whether it is anode- or cathode-supported (400–1800 μm) and a thin electrolyte (8–20 μm). The latter design can lessen ohmic losses in the electrolyte. However, concentration losses

may become significant because of gas diffusion resistances in the electrodes. It has been shown that an anode-supported cell can operate with a wider range of current density and yield higher power densities than a cathode-supported cell (Chan et al., 2001). The couplings of micro processes such as mass and heat transport, chemistry, electrochemistry and charge transfer occurring in the porous electrodes as well as in the electrolyte are crucial for the overall performance of the cell/stack, however, these processes are fairly far from being well understood.

Recknagle et al. (2003) presented a 3D model for prediction the distribution of the gas species, the temperature and the current in a planar SOFC stack. Star-CD was employed and three configurations of co-, counter- and cross-flows were investigated. It was shown that the co-flow configuration generates the most uniform temperature and thus the smallest temperature gradients. However, detailed transport processes in the porous electrodes and electrolyte were not simulated numerically as the PEN structure was treated as a single solid layer. Rather, empirical models were used for potential losses, and chemical species variations due to electrochemical processes were brought into the channel streams as boundary conditions at the PEN-channel interfaces.

In the Fluent based-3D model of Pasaogullari and Wang (2003) which was developed for a planar, electrolyte-supported cell working on hydrogen, transport processes within the PEN structure were modeled. The Butler-Volmer equation with Tafel simplification was used to compute the electrochemical kinetics. The resulting current density was shown for cross-flow configuration, and found to be higher at the areas where the fuel and air channels cross over. Heat or electrochemical enthalpy treatment however was not mentioned.

Klein et al. (2007) recently presented a 2D numerical model for tubular electrolyte-supported SOFC with methane internal reforming, using the commercial package CFD-Ace. The model computed the species partial pressures, current densities and potentials in electronic and ionic phases on the anode side (fuel channel and cermet anode). Small amounts of steam were used to slow down the reforming reaction. Results showed that cooling effects due to the endothermic reforming could be avoided. However, solid carbon was deposited in the anode surfaces due to the Boudouard and methane cracking reactions. This is often a hazard when the ratio steam-to-carbon is lower than unity, reducing the performance, and shortening the cell life.

Zhu et al. (2005) developed a model for a planar, anode-supported cell with co-flow configuration. Gas transport transverse to the channel flows within the porous anode was coupled with the one-dimensional and laminar flow in the fuel channel via mass fluxes at the anode-fuel channel interface. Reforming and shift reactions occurred on the nickel catalyst surface in the cermet anode. Chemical species fractions and surface species coverages were obtained, showing the capability of implementing elementary heterogeneous chemical kinetics in the form of multi-step reaction mechanisms into the SOFC model. However, momentum and energy equations were not taken into account with an isothermal assumption over the whole cell. The impact of the sub-cooling effects on the operating cell therefore was not observed. Carbon formation was not evaluated even though the fuel is free of water at the inlet. The problem of coking was qualitatively evaluated along the three-phase boundary in the very recent work of some of the authors (Janardhanan and Deutschmann, 2007), showing the fact that coking can occur near the inlet even though the supplied methane is humidified.

[Fig. 1 about here.]

In this paper we introduce a model wherein the transport of oxygen ions is modeled by mimicking the effect of the potential by a Fickian diffusion algorithm available in the commercial CFD code Star-CD. The electrical potential is assumed to be uniformly distributed in both sides of the electrolyte due to high electric conductivity of materials. We use an anode-supported planar solid oxide fuel cell to test the model. This work builds on our previous work (Ho et al., 2007), in which hydrogen was the fuel. In the present work internal methane reforming is included, making it possible to study the interaction between different detail processes.

A schematic diagram of the model is shown in Figure 1. Each electrode consists of two layers, namely the current collector and the active layer. The former is used to collect electrons and ensure uniform diffusion of chemical species. It is also a region where catalyzed methane (or natural gas) reforming reactions take place. The latter (also called catalyst layer) is a mixed ionic-electronic conductor containing three-phase boundaries where the electrochemical reactions take place. This layer is very thin ($30 \mu\text{m}$ on the anode side), especially when compared to the total anode thickness ($630 \mu\text{m}$) in the anode-supported SOFC design. Composite electrodes can be used to extend the three-phase boundaries, which contain the electrochemically active sites, giving fuel cells of better performance.

2 Mathematical model

In order to make the simulations economical in terms of demands on time and computational power resources, only a part of a unit cell with co-flow configuration is considered. This part consists of a double gas channel sandwiching a PEN complex. Ideal gas mixtures and incompressible and laminar channel flows due to the small pressure gradients and low Reynolds numbers are also assumed. One of the major challenges of the model is to develop a single domain of calculation, where all equations governing the mass, momentum, species and energy conservations are solved simultaneously. This is the reason for the appearance of the material porosity in the time derivative terms in the mass, species and energy equations below. In the following we give the system of governing equations (Star-CD, 2004). The Einstein summation convention is used. Subscripts i and j denote Cartesian coordinates and therefore take on the values 1, 2 and 3.

2.1 Fluid flow

Mass conservation:

$$\frac{\partial \epsilon \rho}{\partial t} + \frac{\partial \rho u_j}{\partial x_j} = 0 \quad (1)$$

Momentum equation for the channel flow:

$$\frac{\partial \rho u_i}{\partial t} + \frac{\partial}{\partial x_j} (\rho u_j u_i - \tau_{ij}) = -\frac{\partial p}{\partial x_i} + s_i \quad (2)$$

Here, ϵ is the porosity whose values vary between the sub-domains (*e.g.* 1 for the channels, approximately 0 for the electrolyte), ρ is the gas mixture density, u_j is the velocity component in direction x_j , p is the pressure. s_i is

the momentum source components representing the sum of the body and other external forces (*e.g.* buoyancies and rotational forces), which are neglected in this work so that $s_i = 0$. Finally, the stress tensor τ_{ij} is defined for Newtonian fluid and laminar flow as follows:

$$\tau_{ij} = \mu \left(\frac{\partial u_i}{\partial x_j} + \frac{\partial u_j}{\partial x_i} \right) - \frac{2}{3} \rho \frac{\partial u_k}{\partial x_k} \delta_{ij}, \quad (3)$$

where μ is the molecular dynamic viscosity of fluid and δ_{ij} the Kronecker delta. In the porous media namely the electrodes, the momentum balance of the gas permeation obeying Darcy's law is considered as the simplified momentum equation, hence replacing Eq. (2):

$$\frac{\partial p}{\partial x_i} = -K_i u_i, \quad (4)$$

where u_i is the superficial velocity in direction x_i , defined as the volume flow rate divided by the total cross sectional area. $K_i = \alpha_i |u| + \beta_i$ is the porous resistance. The coefficients α_i and β_i are functions of the porosity, the pore size of porous media and the gas viscosity. They are assumed to have the same values in the three different orthogonal directions (Bird et al., 2002):

$$\alpha = \frac{1.75\rho(1-\epsilon)}{\epsilon^3 d_p}; \quad \beta = \frac{150\mu(1-\epsilon)^2}{\epsilon^3 d_p^2} \quad (5)$$

where d_p is the pore diameter.

2.2 Mass transfer

Species conservation equation:

$$\frac{\partial \epsilon \rho Y_m}{\partial t} + \frac{\partial}{\partial x_j} (\rho u_j Y_m + F_{m,j}) = s_m \quad (6)$$

Here, Y_m is the mass fraction of species m , s_m is the rate of mass production or consumption of species m per unit volume due to chemistry and/or electrochemistry. $F_{m,j}$ is the diffusive mass fluxes of species, which are modeled using Fick's law. In Star-CD it is given in the form where thermal effects are taken into account, as follows:

$$F_{m,j} = -\rho D_{m,j} \frac{\partial Y_m}{\partial x_j} - \rho D_{T,j} \frac{\partial \ln T}{\partial x_j} \quad (7)$$

where $D_{m,j}$ and $D_{T,j}$ are the mass and thermal diffusion coefficients, respectively. However, the thermal effects on mass diffusion are not included in the present work since it is negligible compared to the first term on the right hand side of Eq. (7) under relevant conditions. The diffusion coefficient is a combination of the ordinary binary and the Knudsen diffusions, modeled as:

$$\frac{1}{D_1} = \frac{1}{D_{12}} + \frac{1}{D_{1K}}, \quad (8)$$

where D_1 the diffusion coefficient of species 1, D_{12} is the ordinary binary diffusion coefficient of species 1 in 2 and D_{1K} is the Knudsen diffusion coefficient of species 1. The two latter coefficients are defined as:

$$D_{12} = 1.858 \cdot 10^{-7} \sqrt{\frac{1}{M_1} + \frac{1}{M_2}} \frac{T^{3/2}}{p \sigma_{12}^2 \omega_D} \quad (9)$$

and

$$D_{1K} = \frac{d_p}{3} \sqrt{\frac{8RT}{\pi M_1}}, \quad (10)$$

where M_1 and M_2 are the molecular weights (g mol^{-1}) of species 1 and 2 respectively, p is the total pressure (atm), σ_{12} and dimensionless ω_D are Lennard-Jones parameters which can be found in common textbooks (Bird et al., 2002), T is the temperature (K) and R is the universal constant of gas ($\text{J kg}^{-1} \text{K}^{-1}$).

In porous media with the pore diameter much larger than the mean free path of gas molecules the binary diffusion dominates over the Knudsen diffusion

in determining the overall diffusion coefficient. However, if the diffusion is taking place in small pores, the collisions between the diffusing molecule and the pore walls become more frequent than collisions with other gas molecules and the term involving the Knudsen diffusion in Eq. (8) would be dominant. Both diffusion mechanisms may be relevant simultaneously in common SOFC porous electrodes. However, in such media, the diffusion should be also affected by the micro-structure of the materials. An effective diffusion coefficient is therefore used:

$$D_1^{\text{eff}} = \frac{\epsilon}{\tau} D_1, \quad (11)$$

where τ is the tortuosity.

2.3 Heat transfer

Enthalpy equation for a fluid mixture:

$$\frac{\partial}{\partial t} (\epsilon \rho h_t) + \frac{\partial}{\partial x_j} (\rho u_j h_t + F_{h,j}) = \frac{\partial p}{\partial t} + u_j \frac{\partial p}{\partial x_j} + \tau_{ij} \frac{\partial u_i}{\partial x_j} + s_h - s_c \quad (12)$$

Here, s_h is energy sources which may include the heat release due to *e.g.* ohmic resistances and radiation, s_c is chemical energy sources representing endothermic/exothermic chemical and electrochemical processes, $F_{h,j}$ is diffusive energy fluxes. And, $h_t = \bar{c}_p T - c_{p,0} T_0$ is the thermal enthalpy, where \bar{c}_p and $c_{p,0}$ are the specific heat at temperature T and T_0 , respectively.

For solids and fluids of constant density, the specific internal energy, e , is solved instead of h_t . Moreover, in such a case, the first and the second pressure-related terms on the right hand side of Eq. (12) are negligible when compared to other

terms. Eq. (12) then becomes:

$$\frac{\partial}{\partial t}(\epsilon\rho e) + \frac{\partial}{\partial x_j}(\rho u_j e + F_{h,j}) = \tau_{ij} \frac{\partial u_i}{\partial x_j} + s_h - s_c, \quad (13)$$

where $e = \bar{c}T - c_0T_0$. \bar{c} and c_0 are the constant-volume specific heat of the fluid mixture/material at temperature T and T_0 , respectively¹. The diffusive thermal fluxes are the combination of Fourier's conduction and the heat brought by the diffusive mass fluxes, defined as:

$$F_{h,j} = -k \frac{\partial T}{\partial x_j} + \sum_m h_{t,m} F_{m,j}, \quad (14)$$

where k is the thermal conductivity and $h_{t,m}$ is the thermal enthalpy of species m .

3 Modeling of chemistry and electrochemistry

3.1 Modeling of chemistry

Internal reforming of methane (Eq. (15) below) can take place in solid oxide fuel cells operating at high temperatures (800–1000°C). This is one of the advantages of this type of fuel cell compared to others. The presence of the reforming and shift reactions can impact the thermal balance of a cell during operation both positively and negatively. Since the endothermic reforming reactions can suppress the temperature rising in the SOFC itself, extra use of air in the cathode side to reduce the temperature of the cell can be cut down. On the other hand, since the reforming reaction is strongly endothermic, localized reduction of temperature may occur in the cell, leading to high

¹ \bar{c} gets the mean value at 1073K in the present simulations

thermal stresses.



The nickel particles of an anode (*e.g.* Ni-YSZ) function not only as an electronic conductor, but also as a catalyst of the reforming reaction. The heterogeneous reforming reaction is supposed to occur on the Ni-surface in the porous anode support, as well as in the three-phase boundary layer where Ni-particles are also present. The chemical species adsorption to and desorption from the Ni-surface are crucial processes of the reaction mechanism. The free surface of Ni-particles, therefore, contributes to the reaction rate. The reforming reaction rate (Nagata et al., 2001):

$$R_{\text{re}} = 1.75 \left(\frac{p_{\text{CH}_4}}{101325} \right)^{1.2} W_{\text{Ni}} \exp \left(\frac{-57840}{RT} \right), \quad (17)$$

where R_{re} is computed in $\text{mol m}^{-3} \text{s}^{-1}$, p_{CH_4} (Pa) is the partial pressure of methane and W_{Ni} is the Ni load, given in g m^{-3} as the diameter and thus the specific surface area of Ni-particles is not available.

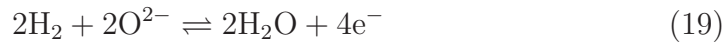
However, within the anode active layer, in addition to the reforming reaction the electrochemical reactions also take place at the three-phase boundaries, causing the appearance of many species simultaneously. The free surface of Ni-particles where methane can adsorb is less due to these species and the reforming reaction rate therefore decreases. The rate is assumed to be two orders lower in this zone compared to that in the support zone in our model. Moreover, since the operating temperature of the cell is high, some homogeneous reforming reactions can probably take place in the gas phase, within the fuel channel. A rate with three orders lower is assumed in the fuel channel.

The reforming reactions produce CO and H₂. H₂ is then oxidized at the

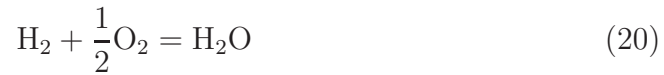
three-phase boundaries to produce electricity, whereas CO either takes part in the electrochemical reaction or further shifts into CO₂ via the shift reaction (Eq. (16)). However, in a system where both H₂ and CO are present the oxidation of the former is dominant over that of the later. Therefore, in this work CO is supposed to only take part in the shift reaction, which is kinetically strong and hence assumed to always be in equilibrium. The shift reaction will run forward in case $K > (p_{\text{CO}_2}p_{\text{H}_2})/(p_{\text{CO}}p_{\text{H}_2\text{O}})$, where K is the equilibrium constant, producing further CO₂ and H₂ while consuming CO and H₂O. The reaction runs backward in the opposite case.

3.2 Modeling of electrochemistry

In solid oxide fuel cells with composite electrodes, O₂ reduction reaction takes place in the cathode active layer (Eq. (18)). On the anode side fuel oxidation reactions take place. H₂ is the only electrochemically active fuel species, its oxidation reaction is assumed to take place in the anode active layer (Eq. (19)).



The overall cell reaction is:



The two half-electrochemical reactions can more generally be written:



The transfer current is calculated as the difference between the currents due to the forward and the backward reactions. For a single-step reaction mechanism

this results in the well-known Butler-Volmer equation (detailed derivation can be found in common textbooks (Bagotsky, 2006; Chen, 2003)):

$$j = A_{ac}i_0 \left\{ \exp\left(\beta \frac{nF\eta}{RT}\right) - \exp\left[-(1-\beta) \frac{nF\eta}{RT}\right] \right\} \quad (22)$$

where j is the transfer current per unit volume of active layer, A_{ac} is the electrochemically active area per unit volume in either the cathode or the anode, i_0 is the exchange current density, which is the exchange current per unit interfacial area due to the forward and backward electrode reactions at the equilibrium potential, β is the transfer coefficient or symmetry factor, varying between 0 and 1 depending on the transition state in the electrochemical reaction, for fuel cell applications $\beta \approx 0.5$, n is the number of electrons participating in the electrochemical reaction, which is 2 for the reaction of Eq. (20), F is Faraday's constant and η is the activation overpotential. Note that j is positive for anode where H_2 oxidation is dominant and negative for cathode electrode where O_2 reduction is dominant.

The activation overpotential for an electrode is defined as:

$$\eta = \Delta\Phi - E_{\text{rev}} \quad (23)$$

where $\Delta\Phi = \Phi_e - \Phi_i$ is the electric potential difference between electronic and ionic phases of the composite electrode, and $E_{\text{rev}, i}$ is the reversible potential of electrode i . The latter is the electric potential difference between the two phases at equilibrium, and can for the half cell reactions of the cathode and anode be written (e.g. Raff, 2001):

$$E_{\text{rev},c} = \frac{1}{4F} (\mu_{\text{O}_2} - 2\mu_{\text{O}_c^{-2}}) \quad (24)$$

$$E_{\text{rev},a} = \frac{1}{2F} (\mu_{\text{H}_2\text{O}} - \mu_{\text{H}_2} - \mu_{\text{O}_a^{-2}}) \quad (25)$$

where μ is the chemical potential.

The reversible potential of the cell can be obtained by combining those electrode equilibrium potentials and in assuming $\mu_{\text{O}_c^{-2}} = \mu_{\text{O}_a^{-2}}$, as follows:

$$\begin{aligned} E_{\text{rev}} &= E_{\text{rev},c} - E_{\text{rev},a} = \frac{1}{4F} (\mu_{\text{O}_2} - 2\mu_{\text{O}_c^{-2}}) - \frac{1}{2F} (\mu_{\text{H}_2\text{O}} - \mu_{\text{H}_2} - \mu_{\text{O}_a^{-2}}) \\ &= E_0 + \frac{RT}{2F} \ln \left(\frac{p_{\text{H}_2,a}}{p_{\text{H}_2\text{O},a}} \right) + \frac{RT}{4F} \ln p_{\text{O}_2,c} \end{aligned} \quad (26)$$

where $E_0 = -\Delta G^0/2F$ with $\Delta G^0 = \mu_{\text{H}_2\text{O}}^0 - \mu_{\text{H}_2}^0 - \mu_{\text{O}_2}^0/2$ is the standard Gibbs free energy change of the cell reaction and we have assumed ideality of the gaseous species by writing: $\mu_i = \mu_i^0 + RT \ln p_i$. Equation (26) is simply the Nernst equation for the cell.

In order to evaluate the reversible electrode potentials, a reference potential, E_{ref} , is defined, so that Eqs. (24) and (25) become:

$$E_{\text{rev},c} = E_{\text{ref}} + \frac{1}{4F} (\mu_{\text{O}_2}^0 - 2\mu_{\text{O}_c^{-2}}) + \frac{RT}{4F} \ln p_{\text{O}_2} \quad (27)$$

$$E_{\text{rev},a} = E_{\text{ref}} + \frac{1}{2F} (\mu_{\text{H}_2\text{O}}^0 - \mu_{\text{H}_2}^0 - \mu_{\text{O}_a^{-2}}) + \frac{RT}{2F} \ln \left(\frac{p_{\text{H}_2\text{O}}}{p_{\text{H}_2}} \right) \quad (28)$$

The concentration and chemical potential of oxygen ions in the electrolyte are required for evaluation of the reversible electrode potentials. However, by choosing an appropriate reference potential so that the sum of the first two terms on the right-hand-side of Eq. (27) vanishes, Eqs. (27) and (28) become:

$$E_{\text{rev},c} = \frac{RT}{4F} \ln p_{\text{O}_2} \quad (29)$$

$$E_{\text{rev,a}} = -E_0 + \frac{RT}{2F} \ln \left(\frac{p_{\text{H}_2\text{O}}}{p_{\text{H}_2}} \right) \quad (30)$$

We note that this reference potential has been assigned different values in the fuel cell literature. For example, it may be chosen so that the equilibrium potential of the cathode vanishes and that of the anode becomes equal to the reversible cell potential (Zhu and Kee, 2007), or such that the equilibrium potential at the anode becomes zero and that at the cathode equal to the reversible cell potential (Shi et al., 2007; Wang, 2004).

In case of low activation losses, applying the truncated Taylor series $e^x \approx 1 + x$ to Eq. (22) gives the kinetics of the two half charge-transfer reactions:

$$r = k_0 |\eta| \quad (31)$$

where $r = |j|/F$ is the reaction rate, computed in $\text{mol m}^{-3} \text{s}^{-1}$ and $k_0 = 2A_{ac}i_0/RT$ is the rate coefficient.

Incorporating Eqs. (23), (29) and (30) into Eq. (31), we have the reaction rates for O_2 reduction reaction at the cathode active layer:

$$r_c = - \left[\Delta\Phi_c - \frac{RT}{4F} \ln p_{\text{O}_2} \right] k_{0,c} \quad (32)$$

and H_2 oxidation reaction at the anode active layer:

$$r_a = \left[\Delta\Phi_a + E_0 - \frac{RT}{2F} \ln \left(\frac{p_{\text{H}_2\text{O}}}{p_{\text{H}_2}} \right) \right] k_{0,a}. \quad (33)$$

At present, as a simplification, we assume that $k_{0,c} = k_{0,a}$, but this is not necessary.

The transfer of oxygen ions across the electrolyte membrane obeys the Nernst-

Planck equation:

$$i = -DzF \left(\frac{\partial C_{ox}}{\partial x} + zC_{ox} \frac{F}{RT} \frac{\partial \Phi_i}{\partial x} \right) \quad (34)$$

where i ($\text{C m}^{-2} \text{ s}^{-1}$) is the current density due to the flow of oxygen ions, C_{ox} (mol m^{-3}) is the oxygen ion concentration, $z = 2$ is the oxygen ion valence, T is the temperature and Φ_i (V) is the electric potential of the ionic phase. Subscript i signifies “ionic” or “ionic phase”. The first term represents Fickian diffusion in the presence of a concentration gradient, and the second ohmic transport in the presence of an electric potential gradient.

If one assumes that the charge transport is largely ohmic, and C_{ox} is approximately constant, the first term becomes negligible, and the current density, in terms of $C_{ch} = -zFC_{ox}$ becomes:

$$i = DzC_{ch} \frac{F}{RT} \frac{\partial \Phi_i}{\partial x} = D \frac{\partial zC_{ch} \frac{F}{RT} \Phi_i}{\partial x} \quad (35)$$

where we have made use of the fact that C_{ch} is constant in the last equation.

Comparing this expression with the Fickian term in Eq. (34), which is the first term on the right-hand-side, we see that if we define an “effective concentration”, C :

$$C \equiv zC_{ch} \frac{F}{RT} \Phi_i \quad (36)$$

to represent the electric potential and then use Fickian diffusion to model a field-driven charge transport in the electrolyte. C is positive in this paper, since Φ_i is negative. However, this may not always be so. Any problems arising from operating with negative values of C can be solved by adding an arbitrary constant to the left-hand-side of Eq. (36), since we are only dealing with gradients or differences of both C and Φ_i .

In fact, in this paper we do not yet attempt to use the physical diffusion coefficient, rather we fit D to obtain physically realistic results. This makes us free to convert potential over the electrolyte to an equivalent charge concentration by just using a unit conversion coefficient, f , while incorporating the other constants in the fitted value of D . We then obtain:

$$dC = d\Phi_i \left(\frac{dC}{d\Phi_i} \right) = d\Phi_i f \quad (37)$$

where f takes on the value -1 if C is in Fmol m⁻³, and -96487 if C is in C m⁻³.

Using Eq. (37), Ohm's law can be written:

$$i = -\lambda \frac{\partial \Phi_i}{\partial x} = -\frac{\lambda}{f} \frac{\partial C}{\partial x} = D \frac{\partial C}{\partial x} \quad (38)$$

which has the form of Fick's first law with $D = -\lambda/f$, where λ is the ionic conductivity of the electrolyte material, is a diffusion coefficient acting on C .

Equation (38) makes it possible to use the Fickian diffusion algorithm in-built in the commercial software to model the ion transport in the electrolyte.

Physically the potential gradient, represented by the gradient of C , and the two electrode overpotentials will, in the steady state, adjust to give the same charge flow per unit cell area due to the three consecutive in-series processes:

- (1) electrochemical reaction at the cathode
- (2) charge flow through the electrolyte
- (3) electrochemical reaction at the anode.

To simulate this we repeat the following iterative procedure until the profiles for C have converged:

- Assume initial profiles for C , giving $\Delta\Phi_c$ and $\Delta\Phi_a$,

- compute the rates of electrochemical reactions from Eqs. (32) and (33),
- obtain new profiles for C .

Please note that although we in this way have chosen a quantity C to represent the electric potential, and call it a “concentration” due to our use of a Fickian diffusion form, this does not mean that we claim that the electric potential at a given point in space can be related to the local concentration of charge. The potential-charge distribution relation can only be found by solving the Poisson equation.

The cell voltage is taken as the electric potential difference between cathode and anode current collectors. This is in line with the assumption of most other workers (Bessler et al., 2007; Zhu et al., 2005; Zhu and Kee, 2007; Wang, 2004) but we acknowledge that this probably will not be precisely true if the two electrodes consist of different materials, as they do here. Under temperature gradients in the cell, thermocouple effects may arise as different thermoelectric voltages are generated in the two electrodes. Such effects should only be relatively minor in our system, thermoelectric voltages typically being only small in comparison with our cell voltage. We also consider that, in practise, the two electrodes are in intimate electrical contact with interconnects that consist of the same material on the anode and cathode sides. We further assume the electrode potentials to be constants due to large electrical conductivity of the materials. Additionally, and for simplicity, we fix the concentration of electrons as constant in the active layers. The electric potentials of the electronic phase therefore become uniform throughout the electrodes. As a consequence, the cell voltage can be calculated by:

$$E_{\text{cell}} = \Phi_{e,c} - \Phi_{e,a} \quad (39)$$

where $\Phi_{e,c}$ and $\Phi_{e,a}$ are the potentials in the anode and cathode active layers, respectively, which are prescribed the values of $\Phi_{e,c} = -1.0$ V and $\Phi_{e,a} = -1.7$ V, for instance, for an operating cell voltage of 0.7 V.

4 Computational grid and simulation techniques

The finite volume method-based mesh is generated for the whole computational domain (Figure 2). The cell length is evenly divided into 200 elements. In the direction normal to the PEN plane (y -direction), the electrolyte consists of 4 elements, the cathode current collector (CCC) and the cathode active layer (CCL) consist of 2 elements each, and finally the anode current collector (ACC) and the anode active layer (ACL) consist of 5 elements each. The whole domain consists of 5200 elements. The mesh is considered to be fine enough to capture all the transport, chemical and electrochemical processes occurring in the cell especially in the PEN complex. Cell component dimensions can be found in Table 1. With an under-relaxation factor of 0.95 chosen for species solvers, it takes approximately 3 hours to complete one simulation on a standard laptop. In principle the model is developed for 3D problems. However, since only one mesh element is generated in the z -direction, it becomes 2D in this study.

[Fig. 2 about here.]

[Table 1 about here.]

5 Model Validation

It was verified that the model results are independent on the mesh size. A comparison of the temperature resolved with two different mesh sizes was performed and is presented in Figure 3. The fine mesh was presented above (*i.e.* 5200 elements). The coarse mesh of 1000 elements is generated similarly to the fine one. However, it consists of 50 (instead of 200) elements in the cell length direction and 2 (instead of 5) elements in the thickness direction of both ACC and ACL. In order to save computational time, internal reforming is not included in the case for which mesh-independence was tested. The fuel composition at the inlet consists of 70% H₂ and 30% H₂O. Other parameters can be found in Tables 2 and 3 below. The fuel channel temperature curves resulting from the two meshes show a very good coincidence, indicating the consistency of the model results regardless of the mesh size. However, the fine mesh was chosen and used throughout this work because of its better capability of capturing small-scale variations.

[Fig. 3 about here.]

It is rather difficult to find experimental studies in the literature where sufficient experimental detail is given to simulate specific cases for model validation. However, we can show that our simulations give results globally consistent with experiment. To do this we carried out simulations at a range of operating voltages, changing the electric potential difference between the electrodes. The results are shown in Figure 4 as curves of both voltage and power density versus the current density. The trends of these curves are completely consistent with experimental data in the literature (e.g. Gorte et al., 2002;

Zhu and Kee, 2003). The rapid drop in the voltage and power density at high current densities is caused by fuel deficiency.

[Fig. 4 about here.]

6 Results and discussion

Table 2 contains model parameters. The boundary and operating conditions can be found in Table 3. The distribution of resulted velocities in the x - y plane is presented in Figure 5. High magnitude in the air channel, low magnitude in the fuel channel and approximate zero magnitude in the PEN structure can be seen.

[Table 2 about here.]

[Table 3 about here.]

[Fig. 5 about here.]

[Fig. 6 about here.]

The evolution of any species can be visualized separately with Star-CD post-processing. However, since many of them are involved in the chemical and/or electrochemical reactions occurring simultaneously it is easier to observe them when they all are plotted together in a single figure. The concentrations of five species in the fuel channel, therefore, are extracted and re-plotted in Figure 6. As can be seen, in coming CH_4 is rapidly reformed with most of it consumed within the first half of the channel length. Considering the H_2O , its concentration is decreasing near the entrance as it is consumed in the reforming reaction.

However, at about 20% of the channel length its production by the electrochemical reaction becomes dominant, causing its concentration to increase to maximum value at the outlet. CO is shifted toward production of CO₂ and further H₂. The fuel utilization is 66.7% in this case. Figures 7 and 8 show the distribution of chemical species across the thickness of the cell. For H₂, the concentration in the porous anode is higher than that in the fuel channel near the entrance (Fig. 7) since the reforming reaction is occurring mainly within the Ni-catalyzed anode. However, the opposite trend is found near the outlet (Fig. 8) where H₂ is oxidized and all CH₄ reacted away. Nevertheless, its gradient which is the greatest compared to that of other species is still small, making the porous anode acceptable for species diffusion. For other species (*e.g.* H₂O, CH₄), concentration gradients can also be observed. However, in the porous structure they are insignificant because of strong mass diffusion within the porous media of 40% porosity and 2 μm pore diameter. The heat associated with enthalpies of chemistry and/or electrochemistry is of interest and displayed in term of temperature in Figures 9 and 10.

[Fig. 7 about here.]

[Fig. 8 about here.]

Electrochemical processes in solid oxide fuel cells release heat heating up the cell. Extra air flow is one approach to regulating the temperature evolution. However, direct internal reforming of natural gas or methane is another approach, which may be better in terms of saving thermal energy. In the present simulations, fuel with 10% (in mole) methane is fed to the fuel channel (see Table 3). The endothermic reforming reaction (Eq. (15)) consumes heat as long as methane is present. This creates a zone near the entrance of the channel with

a very low temperature. However, hydrogen with high concentration produced by the reforming and/or by the shift reactions causes its oxidation processes at the anode active layer to proceed faster. Heat is therefore generated, maintaining the cell at a high temperature of operation. Note that all enthalpy processes occur on the anode side. Therefore, the temperature variation on the cathode side is due to the conduction of the anode-membrane-cathode complex only. As can be seen from Figure 9, the cell length can be divided into two zones based on the relative position of the two channel temperature curves. In the first zone, near the entrance, the air prevents the cell from extreme sub-cooling due to methane reforming, maintaining a high operating temperature. However, in the second zone, the air suppresses the rapid increase of the temperature due to the electrochemical process, keeping the cell at an acceptable thermal stress level. The temperature in the membrane is slightly higher than that in the fuel channel because of the exothermic electrochemical reaction. Since the temperature in the electrodes is not much different from that in the membrane its profile along the cell length is not displayed here. The net increase of temperature in the cell is 184K and the temperature drop near the entrance is approximately 73K.

[Fig. 9 about here.]

[Fig. 10 about here.]

Figure 10 presents the local temperature across the cell thickness at three different positions (10, 50 and 90% cell length). Variations of temperature across the thickness of the fuel channel and the PEN structure are negligibly small. This is probably due to factors such as reforming and shift reactions happening throughout the anode compartment, strong diffusion of chemical

species carrying chemical/electrochemical heat and high thermal conduction of the PEN material. However, variations across the air channel thickness are much stronger, which is probably due to high velocity and thus low residence time of the air. The maximum and average differences of temperature across the cell thickness are 56 K (near the entrance) and 20 K, respectively.

The distribution of the current density along the cell length is shown in Figure 11. Temperature has a strong effect on the kinetics of the electrochemical processes, and hence on the current density. As can be seen, the current density distribution corresponds to the temperature distribution, with a low zone near the entrance and a high zone further downstream of the air and fuel flows. However, near the outlet the current density is seen to drop steeply. This is due to the effect of the fuel depletion. The average current density over the cell length is 0.517 A cm^{-2} , giving an output power density of 0.3619 W cm^{-2} .

[Fig. 11 about here.]

Figure 12 shows the distribution of the resultant "effective concentration" along the anode and cathode active layers. As can be seen, a local minimum appears on the curve for the anode active layer near the entrance of the cell. This is due to the drop of the temperature (see Figure 9), which decreases the diffusion coefficient for oxygen ions through the electrolyte membrane. The continuous curve represents the difference between the curves of the cathode and anode active layers. With the assumption of Eq. (37) ($\Delta C = \Delta \Phi_i f$), it therefore represents the potential drop between the two active layers. This is due to the resistance of the materials to the transport of oxygen ions and hence is called the ohmic overpotential. It is seen to decrease along the cell length, with a local maximum (of 0.153 V) zone near the entrance corresponding to the

sub-cooling zone due to the rapid endothermic methane reforming reaction.

[Fig. 12 about here.]

Figure 13 illustrates potential steps across the cell thickness at the middle of the cell length. Besides the electronic phase potentials of cathode (-1.0 V) and anode (-1.7 V), the ionic phase potential converted from the "effective concentration" is demonstrated. As can be seen, the evolution of the electric potential of the ionic (electrolyte) phase has a similar trend to that found by Bessler et al. (2007). It consists of a nearly linear part resulting from the constant flux of current in the electrolyte membrane.

The reversible electrode potentials $E_{\text{rev,c}}$ and $E_{\text{rev,a}}$ are computed locally using Eqs. (29) and (30) and plotted in terms of $\Phi_{e,c} - E_{\text{rev,c}}$ and $\Phi_{e,a} - E_{\text{rev,a}}$ (dotted thick lines) for easy visualization. The computed activation losses (Eq. (23)) are found to be small, with the average values over the active layer thickness are $\eta_c=0.068$ V and $\eta_a=0.057$ V for the cathode and anode electrochemical reactions, respectively. This yields small errors in using the linear simplification (Eq. (31)) of the Butler-Volmer equation (Chan et al., 2001). The evolution of the electric potential of the ionic phase across the cell thickness stands for the ohmic losses, η_{ohm} . As can be seen from Figure 13, a summation and/or subtraction performance between vectors can retrieve a well-known relation (e.g. Zhu et al., 2005):

$$E_{\text{cell}} = E_{\text{rev,c}} - E_{\text{rev,a}} - \eta_a - |\eta_c| - \eta_{\text{ohm}} \quad (40)$$

where $E_{\text{rev,c}} - E_{\text{rev,a}} = E_{\text{rev}}$ is the reversible potential or the open circuit voltage. It is the maximum potential that can be derived from a cell operating

reversibly and defined by:

$$E_{\text{rev}} = E_0 + \frac{RT}{2F} \ln \left(\frac{p_{\text{H}_2,\text{a}} p_{\text{O}_2,\text{c}}^{0.5}}{p_{\text{H}_2\text{O},\text{a}}} \right) \quad (41)$$

[Fig. 13 about here.]

7 Conclusions

A detailed numerical model has been formulated for, and applied to solid oxide fuel cells. In this model, the transport of oxygen ions was modeled as a Fickian diffusion process mimicking the effect of the potential in the cell. The output cell voltage was based on the electric potential difference between the cathode and anode current collectors, which were fixed as constants. The "effective concentration" of ions was computed and then converted into ionic phase potential, making it possible to determine the potential losses due to activation and ohmic resistance.

A single computational domain covering seven sub-domains (fuel and air channels, anode and cathode current collectors, anode and cathode active layers and electrolyte) was discretized to capture all detailed transport, chemical and electrochemical processes.

The model was applied to an anode-supported planar solid oxide fuel cell with direct internal reforming. Plausible results for the concentration of chemical species, temperature and current density distributions were obtained. The distributions of the electronic and ionic phase potentials across the cell thickness were presented at the middle of the cell length, which enable the activation and ohmic overpotentials to be derived. The derived activation overpotential

was found to be low, confirming the validity of the assumption for linearizing the Butler-Volmer equation. Although further experimental data are needed to validate our model in more detail, it introduces a new tool to understand the effects of the detailed processes involved in the SOFC operation and to predict the optimal operating conditions of SOFCs.

The concentration of electrons was fixed as constant in the active layers for this work. However, it is possible to allow electrons to diffuse inside those layers and also inside the current collectors and the interconnects for instance when applying the model to a whole full cell or stack. This is planned for future work. Thanks to the generality of the governing equations, the model can be used for solid oxide fuel cells with other types of geometrical design, flow conditions and configurations.

Notation

c_p	constant-pressure specific heat (J kg^{-1})
c_v	constant-volume specific heat (J kg^{-1})
C	concentration (C m^{-3} or $F\text{mole m}^{-3}$)
d_p	pore diameter (m)
D	diffusion coefficient ($\text{m}^2 \text{s}^{-1}$)
e	specific internal energy ($\text{J kg}^{-1} \text{K}^{-1}$)
E	potential (V)
F	Faraday constant ($=96487 \text{ C mol}^{-1}$)
$F_{m,j}$	diffusive mass flux of species m ($\text{kg m}^{-2} \text{s}^{-1}$)
$F_{h,j}$	diffusive energy flux component ($\text{J m}^{-2} \text{s}^{-1}$)

h_t	thermal enthalpy ($\text{J kg}^{-1} \text{K}^{-1}$)
$h_{t,m}$	thermal enthalpy of species m (J kg^{-1})
k	thermal conductivity ($\text{W m}^{-1} \text{K}^{-1}$)
K_i	permeability of porous media ($\text{kg m}^{-3} \text{s}^{-1}$)
M	molecular weights (g mol^{-1})
p	pressure (Pa)
r	reaction rate ($\text{mole m}^{-3} \text{s}^{-1}$)
R	universal constant of gas $=8.314 \text{ J kg}^{-1} \text{K}^{-1}$
s_c	chemical energy source ($\text{J m}^{-3} \text{s}^{-1}$)
s_h	energy source ($\text{J m}^{-3} \text{s}^{-1}$)
s_i	momentum source component ($\text{kg m}^{-2} \text{s}^{-2}$)
s_m	rate of production/consumption of species m ($\text{kg m}^{-3} \text{s}^{-1}$)
T	temperature (K)
u_j	velocity component (m s^{-1})
x_j	Cartesian coordinate (m)
Y_m	mass fraction of component m

Greek letters

ϵ	porosity
η	overpotential (V)
μ	dynamic viscosity of gas ($\text{kg m}^{-1} \text{s}^{-1}$)
Φ	potential (V)
ρ	gas mixture density (kg m^{-3})
τ	tortuosity
τ_{ij}	stress tensor (Pa)

Subscripts

$1, 2, m$	species index
a	anode active layer
c	cathode active layer
ch	charge
e	electronic phase
i	ionic phase
i, j, k	Cartesian directions
rev	reversible

Abbreviations

ACC	anode current collector
ACL	anode catalyst layer
CCC	cathode current collector
CCL	cathode catalyst layer

Acknowledgments

Financial support from the NFR through the MSOFC program is gratefully acknowledged.

References

- Aguiar, P., Adjiman, C. S., Brandon, N. P., 2004. Anode-supported intermediate temperature direct internal reforming solid oxide fuel cell. i: model-based steady-state performance. *Journal of Power Sources* 138, 120–136.
- Bagotsky, V. S. (Ed.), 2006. *Fundamentals of Electrochemistry*, 2nd Edition. John Wiley & Sons, Ch. 6.
- Bessler, W. G., Gewies, S., Vogler, M., 2007. A new framework for physically based modeling of solid oxide fuel cells. *Electrochimica Acta* 53, 1782–1800.
- Bird, R. B., Stewart, W. E., Lightfoot, E. N., 2002. *Transport phenomena*, 2nd Edition. John Wiley and Sons, New York.
- Chan, S. H., Khor, K. A., Xia, Z. T., 2001. A complete polarization model of a solid oxide fuel cell and its sensitivity to the change of cell component thickness. *Journal of Power Sources* 93, 130–140.
- Chen, E., 2003. Thermodynamics and electrochemical kinetics. In: Hoogers, G. (Ed.), *Fuel Cell Technology Handbook*. CRC Press, Ch. 3.
- Ciucci, F., Goodwin, D. G., 2007. Non linear modeling of mixed ionic electronic conductors. In: *ECS Transactions*. Vol. 7(1). pp. 2075–2082.
- Fleig, J., 2002. On the width of the electrochemically active region in mixed conducting solid oxide fuel cell cathodes. *Journal of Power Sources* 105, 228–238.
- Fleig, J., 2003. Solid oxide fuel cell cathodes: Polarization mechanisms and modelling of the electrochemical performance. *Annu. Rev. Mater. Res.* 33, 361–382.
- Gorte, R. J., Kim, H., Vohs, J. M., 2002. Novel SOFC anodes for the direct electrochemical oxidation of hydrocarbon. *Journal of Power Sources* 106, 10–15.

- Hao, Y., Goodwin, D. G., 2007. Numerical study of heterogeneous reactions in an sofc anode with oxygen addition. In: ECS Transactions. Vol. 7(1). pp. 1859–1867.
- Ho, T. X., Kosinski, P., Hoffmann, A. C., Wærnhus, I., Vik, A., 2007. Numerical simulation of electrochemical and transport processes in solid oxide fuel cells. In: ECS Transactions. Vol. 7(1). pp. 1901–1908.
- Inui, Y., Ito, N., Nakajima, T., Urata, A., 2006. Analytical investigation on cell temperature control method of planar solid oxide fuel cell. *Energy Conversion and Management* 47, 2319–2328.
- Janardhanan, V. M., Deutschmann, O., 2006. CFD analysis of a solid oxide fuel cell with internal reforming: Coupled interactions of transport heterogeneous catalysis and electrochemical processes. *Journal of Power Sources* 162, 1192–1202.
- Janardhanan, V. M., Deutschmann, O., 2007. Numerical study of mass and heat transport in solid oxide fuel cells running on humidified methane. *Chemical Engineering Science* 62, 5473–5486.
- Kenney, B., Karan, K., 2004. Mathematical micro-model of a solid oxide fuel cell composite cathode. In: *Proceedings Hydrogen and Fuel Cells*. Toronto, Canada.
- Klein, J. M., Bultel, Y., Georges, S., Pons, M., 2007. Modeling of a SOFC fuelled by methane: From direct internal reforming to gradual internal reforming. *Chemical Engineering Science* 62, 1636–1649.
- Lehnert, W., Meusinger, J., Thom, F., 2000. Modelling of gas transport phenomena in SOFC anodes. *Journal of Power Sources* 87, 57–63.
- Li, P. W., Chyu, M. K., 2003. Simulation of the chemical/electrochemical reactions and heat/mass transfer for a tubular SOFC in a stack. *Journal of Power Sources* 124, 487–498.

- Nagata, S., Momma, A., Kato, T., Kasuga, Y., 2001. Numerical analysis of output characteristics of tubular SOFC with internal reformer. *Journal of Power Sources* 101, 60–71.
- Pasaogullari, U., Wang, C. Y., 2003. Computational fluid dynamics modeling of solid oxide fuel cells. In: *The Electrochemical Society Proceedings*. Vol. 7. Pennington, New Jersey, pp. 1403–1412.
- Petruzzi, L., Cocchi, S., Fineschi, F., 2003. A global thermo electrochemical model for SOFC systems design and engineering. *Journal of Power Sources* 118, 96–107.
- Raff, L. M., 2001. *Principles of Physical Chemistry*. Prentice Hall, Upper Saddle River, NJ.
- Recknagle, K. P., Williford, R. E., Chick, L. A., Rector, D. R., Khaleel, M. A., 2003. Three-dimensional thermo-fluid electrochemical modeling of planar SOFC stacks. *Journal of Power Sources* 113, 109–114.
- Shi, Y., Cai, N., Li, C., Bao, C., Croiset, E., Qian, J., Hu, Q., Wang, S., 2007. Modeling of an anode-supported Ni-YSZ||Ni-ScSZ||ScSZ||LSM-ScSZ multiple layers SOFC cell Part I. Experiments, model development and validation. *Journal of Power Sources* 171, 235–245.
- Søgaard, M., Hendriksen, P. V., Jacobsen, T., Mogensen, M., 2006. Modelling of the polarization resistance from surface exchange and diffusion coefficient data. In: *Proceedings of The Seventh European SOFC Forum*. Lucerne.
- Star-CD, 2004. *Version 3.24 Methodology*. CD adapco Group.
- Suwanwarangkul, R., Croiset, E., Fowler, M. W., Douglas, P. L., Entchev, E., Douglas, M. A., 2003. Performance comparison of fick's, dusty-gas and stefan-maxwell models to predict the concentration overpotential of a SOFC anode. *Journal of Power Sources* 122, 9–18.
- Suwanwarangkul, R., Croiset, E., Pritzker, M. D., Fowler, M. W., Douglas,

- P. L., Entchev, E., 2006. Mechanistic modelling of a cathode-supported tubular solid oxide fuel cell. *Journal of Power Sources* 154, 74–85.
- Wang, C. Y., 2004. Fundamental models for fuel cell engineering. *Chem. Rev.* 104, 4727–4766.
- Yakabe, H., Ogiwara, T., Hishinuma, M., Yasuda, I., 2001. 3-D model calculation for planar SOFC. *Journal of Power Sources* 102, 144–154.
- Zhu, H., Kee, R. J., 2003. A general mathematical model for analyzing the performance of fuel-cell membrane-electrode assemblies. *Journal of Power Sources* 117, 61–74.
- Zhu, H., Kee, R. J., 2007. Modeling distributed charge-transfer processes in membrane electrode assemblies with mixed-conducting composite electrodes. In: *ECS Transactions*. Vol. 7(1). pp. 1869–1878.
- Zhu, H., Kee, R. J., Janardhanan, V. M., Deutschmann, O., Goodwin, D. G., 2005. Modeling elementary heterogeneous chemistry and electrochemistry in solid oxide fuel cells. *Journal of The Electrochemical Society* 152, A2427–A2440.

List of Figures

1	Schematic diagram of a unit anode-supported SOFC. ACC and CCC: anode and cathode current collectors, respectively; ACL and CCL: anode and cathode catalyst layers, respectively	36
2	Computational mesh	37
3	Evolution of the temperature along the fuel channel (without internal reforming)	38
4	Working voltage and power density vs. current density	39
5	Velocity profile in the $x-y$ plane (max. magnitude is 3.9 m/s)	40
6	Evolution of the chemical species along the fuel channel	41
7	Distribution of chemical species across the cell thickness at 10% of the cell length	42
8	Distribution of chemical species across the cell thickness at 90% of the cell length	43
9	Evolution of the temperature along the cell length	44
10	Distribution of the temperature across the cell thickness	45
11	Distribution of the current density along the cell length	46
12	Distribution of the "effective concentration", C , along the cell length	47
13	Electric potential of ionic and electronic phase across the cell thickness at the middle of the cell length. The up-arrow (\uparrow) means positive; the down-arrow(\downarrow) means negative	48

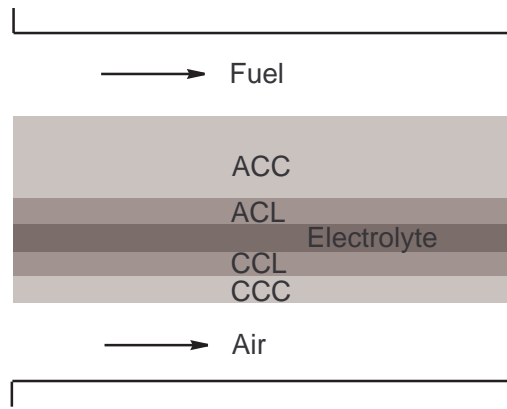


Fig. 1. Schematic diagram of a unit anode-supported SOFC. ACC and CCC: anode and cathode current collectors, respectively; ACL and CCL: anode and cathode catalyst layers, respectively

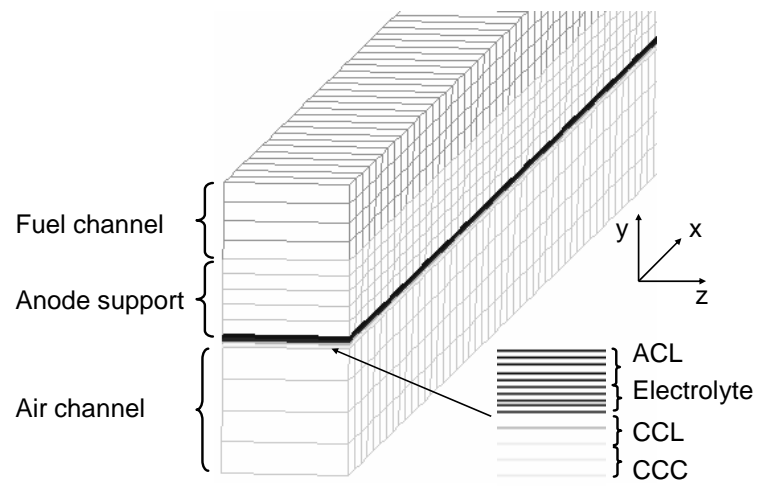


Fig. 2. Computational mesh

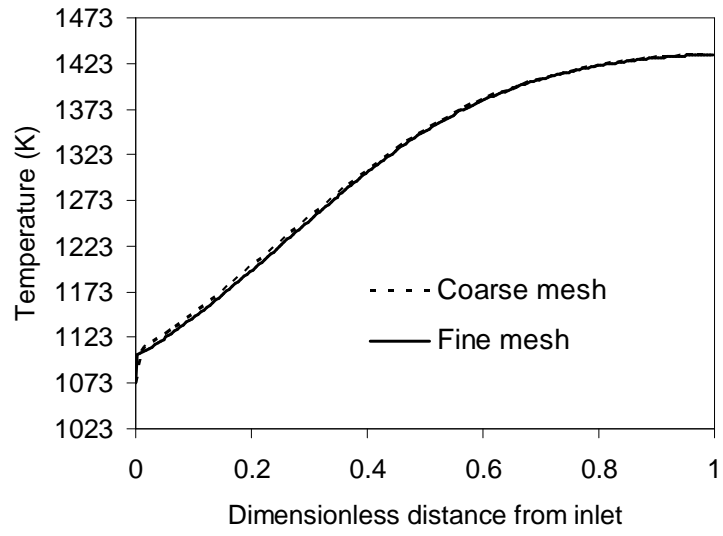


Fig. 3. Evolution of the temperature along the fuel channel (without internal re-forming)

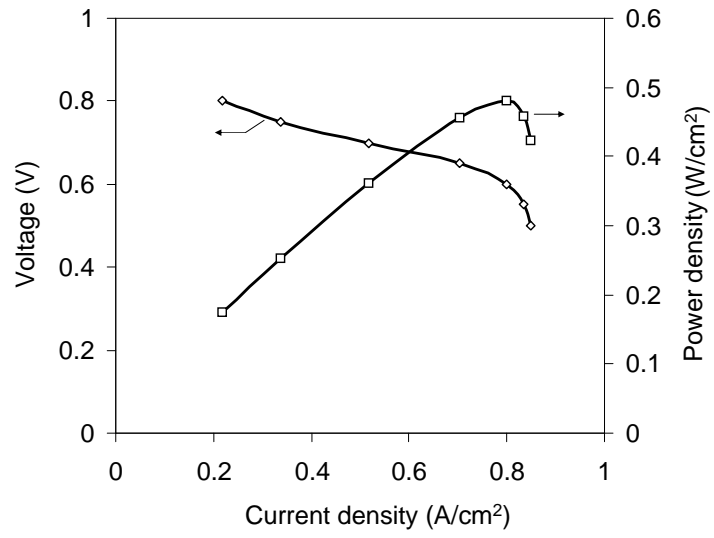


Fig. 4. Working voltage and power density vs. current density

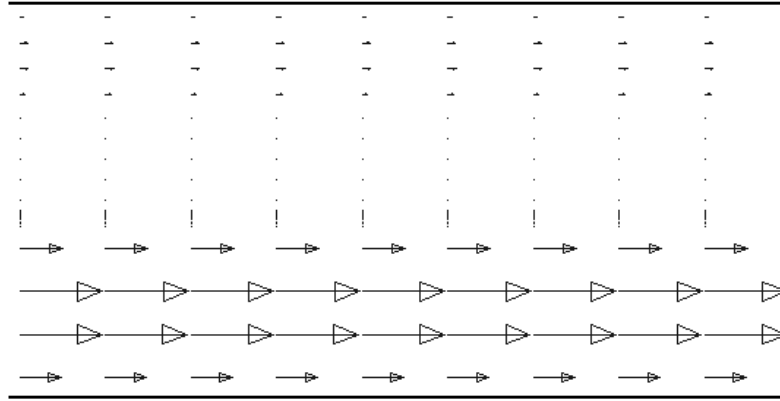


Fig. 5. Velocity profile in the $x-y$ plane (max. magnitude is 3.9 m/s)

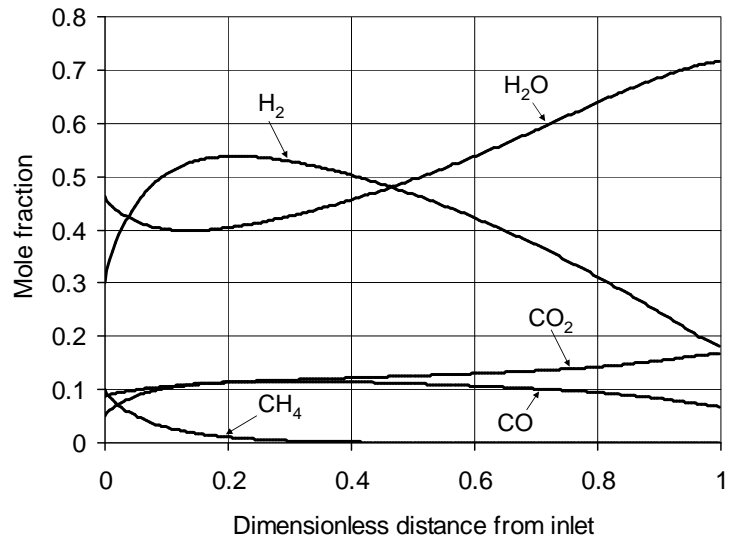


Fig. 6. Evolution of the chemical species along the fuel channel

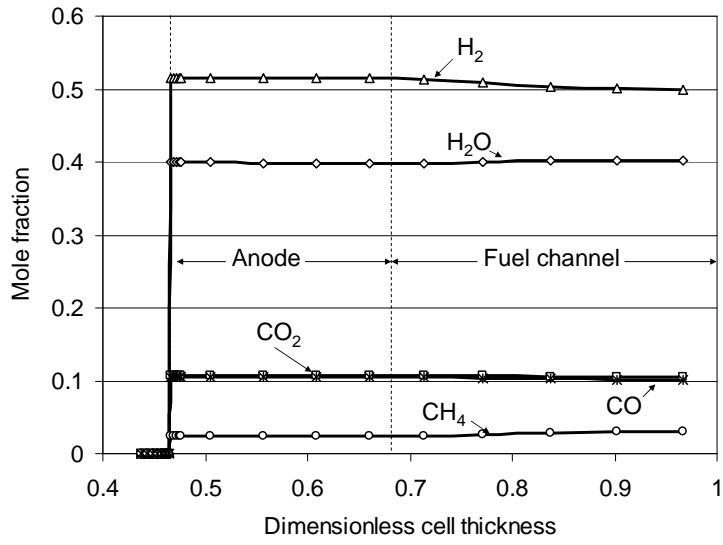


Fig. 7. Distribution of chemical species across the cell thickness at 10% of the cell length

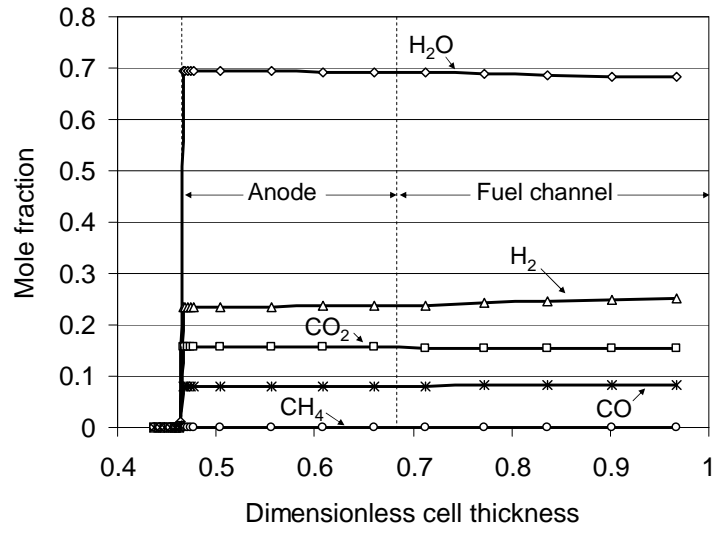


Fig. 8. Distribution of chemical species across the cell thickness at 90% of the cell length

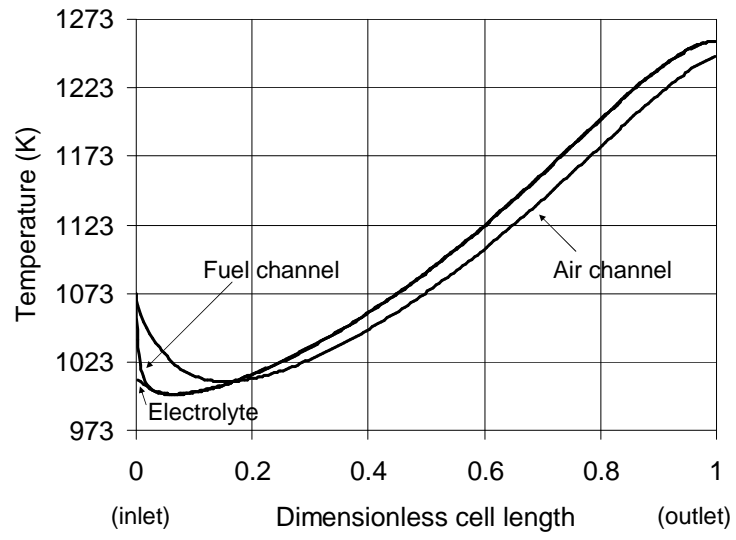


Fig. 9. Evolution of the temperature along the cell length

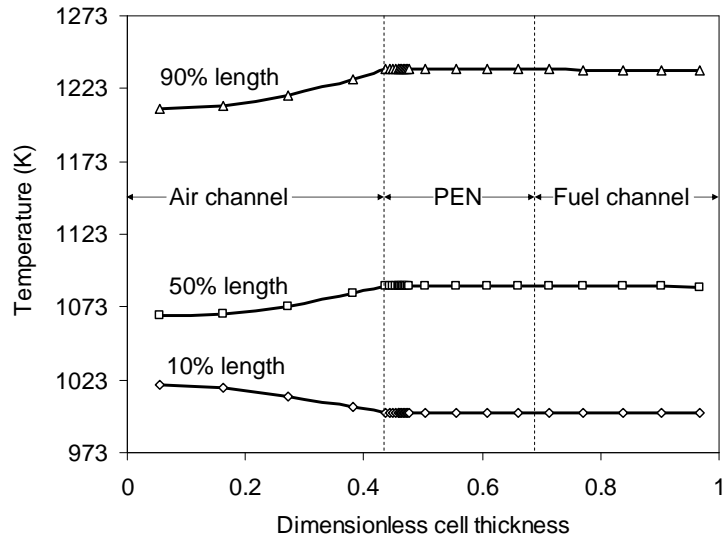


Fig. 10. Distribution of the temperature across the cell thickness

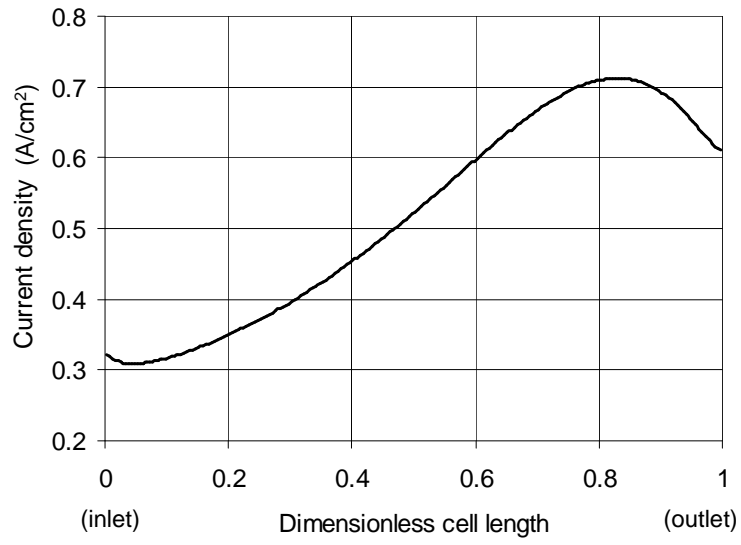


Fig. 11. Distribution of the current density along the cell length

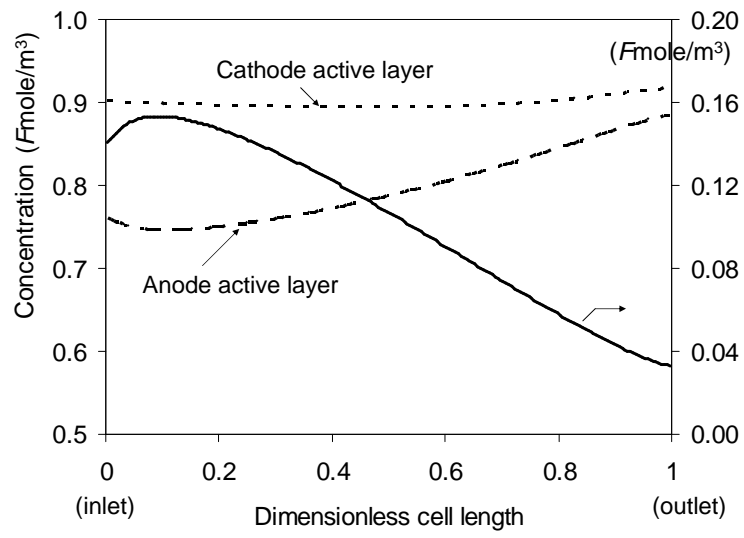


Fig. 12. Distribution of the "effective concentration", C , along the cell length

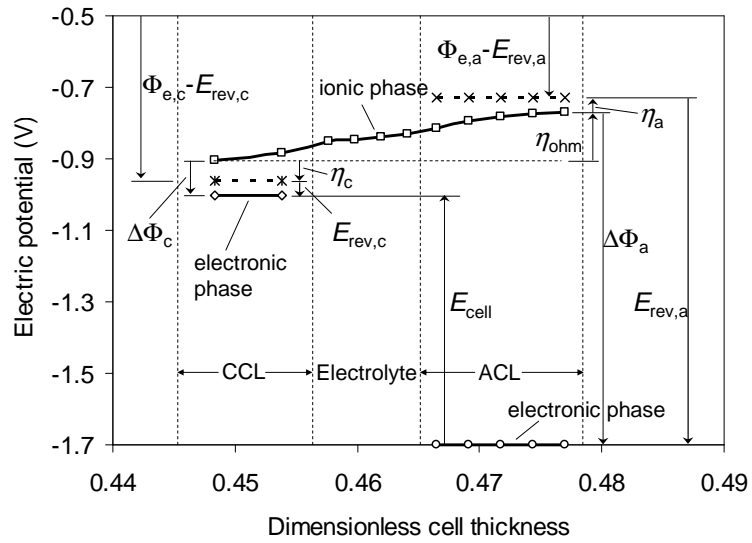


Fig. 13. Electric potential of ionic and electronic phase across the cell thickness at the middle of the cell length. The up-arrow (\uparrow) means positive; the down-arrow (\downarrow) means negative

List of Tables

1	Dimensions of cell components	50
2	Physical properties of cell components	51
3	Boundary and operating conditions	52

Table 1
 Dimensions of cell components

Parameters	Value	Units
Cell length	100	mm
Cell width	1	mm
Air channel height	1	mm
Fuel channel height	0.6	mm
Anode support thickness	0.6	mm
Anode active layer thickness	30	μm
Cathode active layer thickness	25	μm
Cathode current collector thickness	25	μm
Electrolyte thickness	20	μm

Table 2
Physical properties of cell components

Parameters	Value	Units
Thermal conductivity, k		
Anode/cathode/electrolyte	4/4/10	$\text{W m}^{-1} \text{K}^{-1}$
Oxygen charge diffusion coefficient, D		
in the electrolyte	$0.881\exp(-11000/T)$	$\text{m}^2 \text{s}^{-1}$
Anode/cathode active layer	$0.308\exp(-11000/T)$	$\text{m}^2 \text{s}^{-1}$
Anode/cathode porosity, ϵ	0.4/0.3	
Anode/cathode tortuosity, τ	1.6/1.6	
Anode/cathode pore diameter, d_p	2/1	μm
Anode active layer density (Ni 50%wt.)	4300	kg m^{-3}

Table 3
Boundary and operating conditions

Parameters	Value and units
Fuel inlet	
Velocity	0.3 m s ⁻¹
Temperature	1073 K
Fuel compositions	H ₂ O 46.3%, H ₂ 30%, CH ₄ 10%, CO 5%, CO ₂ 8.7%
Air inlet	
Velocity	2.93 m s ⁻¹
Temperature	1073 K
Air compositions	O ₂ 21%, N ₂ 79%
Side walls	symmetrical
Wall (others)	no-slip, adiabatic
Cell voltage	0.7 V
Rate coefficient, k_0	$1.995 \cdot 10^6 \exp(-50000/RT)$